

Anoxic weathering of mafic oceanic crust promotes atmospheric oxygenation

Drew D. Syverson^{1*}, Christopher T. Reinhard^{2,3,4}, Terry T. Isson^{1,5},
Cerys Holstege¹, Joachim Katchinoff¹, Benjamin M. Tutolo⁶,
Barbara Etschmann⁷, Joël Brugger⁷, Noah J. Planavsky^{1,3}

¹Yale University, Department of Geology and Geophysics, New Haven, CT, USA

²Georgia Institute of Technology, Earth and Atmospheric Sciences, Atlanta, GA, USA

³NASA Astrobiology Institute, Alternative Earths Team

⁴NASA Nexus for Exoplanet System Science (NExSS)

⁵University of Waikato (Tauranga), Faculty of Science & Engineering, NZ

⁶University of Calgary, Department of Geosciences, Calgary, AB, CA

⁷Monash University, Earth, Atmosphere & Environment, Melbourne, VIC, AU

*Corresponding author:

syverson.drew@gmail.com

612-475-0575

210 Whitney Ave, New Haven, CT, USA 06511

Abstract

Phosphorus is an essential element for all known life, and the global phosphorous cycle is widely believed to be a key factor limiting the extent of Earth's biosphere. The size and scope of any biosphere beyond our solar system is similarly likely to be limited by the planetary cycling of bioavailable phosphorus. Continental weathering has long been considered to be the only source of bioavailable phosphorus to the oceans, with submarine hydrothermal processes acting as a phosphorus sink [1]. This opens up the possibility of severe phosphorus limitation on the early Earth prior to the widespread emergence of continental crust above sea level, and further implies that a common class of volatile-rich habitable exoplanet—so called 'waterworlds' [2] — may be biological deserts. However, this framework is based on the behavior of phosphorus in modern hydrothermal systems interacting with pervasively oxygenated deep oceans. Here, we present new experimental results indicating that abiotic carbon dioxide sequestration during anoxic basalt alteration is an efficient source of bioavailable phosphorus. Placing these observations into the context of a simple model of planetary phosphorus-carbon-oxygen mass balance, we suggest that volatile-rich Earth-like planets lacking exposed continents may actually be more likely than Earth to develop robust biospheres that can lead to remotely detectable atmospheric biosignatures [3].

1. Introduction

Phosphorus (P) is a critical component of the genetic and energetic machinery of all life and plays key structural roles in most organisms. Recent debate has bolstered the case that P is not only essential for life on Earth but is also likely central for recognizable biochemistry more broadly [4, 5]. Recent biogeochemical modeling and reconstructions of the evolution of marine phosphate (PO_4^{3-}) concentrations from Earth's rock record have bolstered the case that P has been the ultimate limiting nutrient throughout Earth's history [6-8]. It has also been argued that P would be expected to limit the extent of life on exoplanets where oxygenic photosynthesis has evolved [9]. Therefore, a mechanistic understanding of how the global P cycle has changed through time is crucial both for a basic understanding of the history of life on our planet and in the development of predictive frameworks for the production and maintenance of exoplanet biosignatures.

Continental weathering, an important long-term CO_2 sink regulating planetary climate, is also the only significant source of P to the modern oceans [10]. Submarine weathering of basaltic oceanic crust, while also serving as a long term CO_2 sink, currently acts a significant removal process of P from marine systems [11]. For example, roughly 20% of the P sourced to the oceans today is removed through basalt alteration [10, 12]. The remainder is removed in association with the burial of authigenic apatite, organic P, and iron oxides in marine sediments. Marine PO_4^{3-} concentrations are controlled through time by the interplay between the efficiency of P burial and the magnitude of the P source(s). It has been proposed that anoxic and iron-rich (ferruginous) oceans, which were widespread on the early Earth [13, 14], lead to enhanced P scavenging through adsorption onto iron oxide minerals formed near the oxygenated ocean-atmosphere interface and through the precipitation of reduced iron-phosphate minerals directly from seawater [7, 9, 15].

Phosphorus removal during basalt alteration may have also been enhanced in Earth's past, given that it is likely that oceanic crust weathering played a more significant role in weathering and CO₂ sequestration prior to the emergence of continents above sea level and the proliferation of land plants in terrestrial ecosystems [16, 17]. However, previous work has neglected the possibility that dissolved P may become liberated into seawater during marine weathering of oceanic crust in the absence of dissolved O₂—as a natural result of limited Fe²⁺ oxidation and subsequent P scavenging. Although mid-ocean ridge basalts (MORB) typically do not contain igneous apatite, P⁵⁺ substitutes for Si⁴⁺ in primary silicate minerals [18, 19], and this P may be released during submarine basalt alteration. If operative, this process would reshape our view of the evolution of the P cycle on Earth [9, 16] and would become an important component of attempts to predict planetary P cycling on habitable exoplanets. Here, we provide direct experimental support for the idea that basalt weathering under anoxic marine conditions can be a significant source of bioavailable P to aqueous systems.

2. Methods

2.1 Experimental Design

The experiments utilized an enriched dissolved ²⁹SiO₂ tracer to directly and accurately correlate the extent of primary silicate mineral dissolution with the amount of PO₄³⁻ mobilized into seawater upon reaction with natural submarine basalt under anoxic conditions. Two sets of experiments are presented, one utilizing fresh submarine basalt and one in which the fresh submarine basalt was treated with a reductive dissolution procedure designed to remove pre-existing Fe³⁺-oxides associated with partial oxidation during recovery from the seafloor [20]. Mineral characterization

of the reactant basalt is combined with time-series changes in dissolved PO_4^{3-} and $^{29}\text{SiO}_2$ to allow determination of the efficacy of basalt weathering as a source of critical nutrients under the anoxic conditions characteristic of the early Earth and reducing exoplanet waterworlds. The reduced dissolved P^{3+} species [21] is not considered in this study since the prescribed conditions of the experiments dictate that P^{5+} species, specifically PO_4^{3-} , are thermodynamically stable and that P derived from the dissolution of primary silicate minerals of the reactant basalt exists as P^{5+} [18]. Oxygenated basalt weathering experiments were also conducted in order to demonstrate the removal and retention of dissolved PO_4^{3-} as a consequence of the formation of Fe^{3+} -oxide minerals upon reaction, providing a comparative analysis of PO_4^{3-} mobility with the anoxic experiments.

Two sets of long term basalt-seawater alteration experiments were conducted for over 2000 hours to better quantify the mobility of dissolved inorganic PO_4^{3-} under a range of dissolved O_2 concentrations: (1) anoxic experiments, BA-1 and BA-2, where it is expected that PO_4^{3-} adsorption will be limited due to the lack of Fe^{3+} -oxide mineral formation, all of which were conducted at 25°C (Table 1); and (2) oxygenated experiments, BA-3, BA-4, and BA-5 (Table A1), with concentrations of O_2 at present atmospheric level, in which we demonstrate the process of PO_4^{3-} adsorption onto Fe^{3+} -oxides associated with oxidative alteration of basalt [1, 22]. Experiments BA-3, BA-4, and BA-5 were conducted at 75 , 50 , and 15°C , respectively. All of the experiments were conducted at temperatures elevated with respect to bottom seawater but within the range of temperatures associated with carbonate precipitation in subseafloor upon chemical weathering of the oceanic crust [11, 23].

2.2 Anoxic Basalt Alteration Experiments

The anoxic experiments were prepared, initiated, and maintained under anoxic conditions inside a COY™ anaerobic chamber with an atmosphere composed of 5% H₂:95% N₂. Each anoxic basalt alteration experiment was conducted in a gas-tight 250 mL Pyrex reactor with two gas-tight sampling ports, allowing for direct time-series sampling of the reactor solution without termination of the experiment and for keeping the reaction system closed to external environmental changes. Additionally, each reactor was wrapped in aluminum foil to shield from UV radiation, effectively preventing photo-oxidation of dissolved Fe²⁺ liberated from the dissolution of reactant basalt. Commencement of each experiment began by combination of the reactant basalt with the synthetic seawater and immersion into a temperature-regulated circulating oil bath set at 25 ± 0.1 °C. Solution samples were taken with time to assess the change in the composition of reactant seawater solution over the course of approximately 1500 hours. A typical sampling mass of solution for each sampling session can range between 4 - 8 grams. The first sample, through the sampling line of the reactor, is used as a “bleed” to effectively wash out the sampling tube with experimental solution. The second sample is taken for cations/anions and pH analysis. A third sample may be taken for additional sample solution for additional analysis. In exchange with experimental solution taken from the reactor, an equivalent volume of 5% H₂:95% N₂ atmosphere enters the experimental reactor. After the sampling session, both the intake and extraction valves are closed to keep the experimental system closed to any external changes in the COY™ chamber throughout reaction progress. The cation samples were diluted with trace metal grade 0.1N HCl to prevent metal precipitation effects while the anion samples were diluted accordingly with ultra-pure H₂O (18.2 MΩ).

The reactant solution for each anoxic experiment, BA-1 and BA-2, was prepared with deoxygenated ultrapure H₂O and designed to have concentrations of dissolved components to simulate seawater, but with elevated concentrations of dissolved ²⁹Si-enriched SiO₂, 500 mmol/kg NaCl – 40 mmol/kg MgCl₂ – 16 CaCl₂ mmol/kg – 500 μmol/kg ²⁹SiO₂ (Table 1 and A1). The pH was buffered at 6.5 with the MOPS (3-(N-morpholino) propanesulfonic acid) buffer to effectively preclude changes in pH as a consequence of basalt dissolution and acidity produced from secondary mineral formation. The reactant basalt was recovered from near the axis of the Juan de Fuca Ridge and was separated from the basalt glass and the crystalline fraction, where the crystalline fraction was powdered to achieve maximum reactive surface area to enhance reaction progress, sieved to achieve a distribution between 5-50 μm in grain size. A fraction of the crystalline powdered basalt reactant was treated with a citrate-bicarbonate-dithionite (CBD) reductive dissolution step prior to commencement of the experiments [20]. The CBD method specifically removes pre-existing Fe³⁺-oxides from the natural reactant basalt, which may have a significant effect on the mobility of PO₄³⁻ liberated from basalt upon alteration under anoxic conditions (Table A1). The CBD method does not react with and or dissolve the primary reactant basalt silicate minerals [20]. Thus, the primary P⁵⁺, which resides as a trace element within the primary silicate minerals will remain unreactive (as lattice-bound P⁵⁺ within silicates [18]) upon CBD treatment of the reactant basalt. Further, if any of the P⁵⁺ associated with the secondary Fe³⁺-oxide minerals were to become reduced to P³⁺ [21], the highly soluble P³⁺ would have dissolved within the CBD leachate solution. Once the CBD procedure is terminated, the CBD treated basalt minerals are immediately filtered, cleaned by washing with copious amounts of ultrapure H₂O, and then dried under an anoxic N₂ atmosphere, with the result that any liberated P³⁺ would not be measured by our procedure as being liberated during primary basalt dissolution.

The two experiments, basalt with and without the CBD treatment, BA-1 and BA-2, respectively, were designed to have an elevated water/rock ratio (W/R~65; approximately 250 g of solution + 3.8 g of basalt), where the mass balance of SiO₂ in the experimental system is dominated by reactant basalt ($X_{\text{SiO}_2(\text{Basalt})}^1 \sim 1$). Specifically, the enriched ²⁹SiO₂ spike (500 μmol/kg, ²⁹Si/²⁸Si~100) introduced with the anoxic synthetic seawater was utilized to quantify the degree of silicate dissolution within basalt with reaction progress. The change in the abundance of ²⁹Si relative to ²⁸Si between the dissolved and solid reservoirs (seawater + basalt) is monitored with time, where it is expected that the ²⁹Si/²⁸Si ratio of the solution will decrease with increasing degrees of basaltic silicate dissolution, ultimately approaching the natural ²⁹Si/²⁸Si ratio (~0.05) due to mass balance constraints in the experimental system. This approach is advantageous since the change in the ²⁹Si/²⁸Si ratio in the solution is not affected by secondary mineral formation effects in contrast to observed changes in the total concentration of dissolved SiO₂ [24, 25].

2.3 Oxygenated Basalt Alteration Experiments

Three oxygenated experiments, BA-3, BA-4, and BA-5 were conducted by reacting ground crystalline basalt (~20-250 μm grain size) with a synthetic seawater solution that is enriched in dissolved PO₄³⁻ (25.4 μmol/kg) relative to natural bottom seawater (~2 μmol/kg) to illustrate the effect of adsorption onto pre-existing and incipiently formed Fe³⁺-oxide surfaces upon alteration of the reactant basalt (Table A1). For each experiment, eight identical 30 mL Teflon reactors were designed to have identical water/rock ratios (W/R~10: 10 g of seawater solution: 1 g of basalt

¹ $X_{\text{SiO}_2(\text{Basalt})} = m_{\text{SiO}_2(\text{Basalt})} / (m_{\text{SiO}_2(\text{Basalt})} + m_{\text{SiO}_2(\text{Dissolved})})$, where m designates total moles of SiO₂ for each respective phase, basalt and seawater.

reactant) and all have a headspace (approximately 20 mL) composed of modern atmosphere. The oxygenated reactant seawater was prepared to have a solution chemistry which closely resembles the composition of modern seawater, 500 mmol/kg NaCl – 50 mmol/kg MgCl₂ – 10 CaCl₂ mmol/kg – 50-100 μmol/kg SiO₂. These particular experiments did not implement the ²⁹SiO₂ enriched tracer in the experimental solution but rather used natural abundance reagent-grade SiO₂. In addition, these particular experiments did not use a pH buffer but rather allowed the pH to change as a consequence of mineral dissolution and secondary mineral formation. Each reactor was maintained at 75, 50, and 15 ± 0.1 °C, BA-3, BA-4, and BA-5, respectively, in a shaking water bath, to maintain the experiment at a constant temperature throughout the course of basalt alteration. Over the course of approximately >4000 hours, individual reactors were terminated sequentially with reaction progress to determine the change in composition of the reactant seawater and to monitor changes in mineral speciation and element distribution of the altered basalt relative to the reactant material (see SI for further details of the oxygenated experiments, BA-3 – 5).

2.4 Analytical Measurements

The time-series solution samples taken from each experiment, anoxic and oxygenated, were measured for pH immediately after sampling by use of a Thermo Scientific™ Orion™ PerpHecT™ ROSS™ Combination pH Micro Electrode, which was calibrated with the pH buffers, 4, 7, 10 before each analysis (Table 1 and A1). The error associated with the pH measurement is within ±0.02 log units (2σ). The concentration of the dissolved components of interest and the ²⁹Si/²⁸Si ratio were determined by use of a Thermo Scientific™ Element™ XR inductively coupled plasma mass spectrometer (ICP-MS). Due to the extreme ²⁹Si/²⁸Si ratio of the experimental solution samples (>10) relative to natural material (~0.05), the small effects of isotope

fractionation, which may occur upon basalt alteration and during analysis by ICP-MS, can be neglected [24, 26]. In addition, the large enrichment of dissolved ^{29}Si in solution allows measurement by ICP-MS to be of sufficient resolution to monitor statistically significant changes in the solution $^{29}\text{Si}/^{28}\text{Si}$ ratio (2.6-3% RSD, 1σ) upon reaction with the natural reactant basalt. The relative standard deviation (2σ) of the ICP-MS measurements ranges between 6-10% for P, 1-5% for Fe and Mn, 1-3% for ^{28}Si , ^{29}Si , and ^{30}Si , and 1-2 % for the major cations, Ca^{2+} and Mg^{2+} .

2.5 Geochemical Modeling

The Geochemist's Workbench v. 12.0.4 [27] outfitted with a custom database produced using the DBCreate software package [28] was used to calculate the speciation of the time-series solution samples, the vivianite saturation state (Table A1), and produce the activity diagram plotted in Fig. A2. Thermodynamic data for the speciation of P in solution was taken from Shock, Sassani, Willis and Sverjensky [29], and the solubility of vivianite ($\text{Fe}_3(\text{PO}_4)_2 \cdot 8\text{H}_2\text{O}$) was calculated according to the equation given by Al-Borno and Tomson [30].

2.6 $^{29}\text{Si}/^{28}\text{Si}$ Mass Transfer Systematics

The enriched dissolved $^{29}\text{SiO}_2$ tracer approach was utilized in this study since the change in $^{29}\text{Si}/^{28}\text{Si}$ ratio of the reactant seawater is a reflection only of the dissolution of reactant basalt and not by secondary mineral formation processes [24]. The initially elevated dissolved SiO_2 concentration of the anoxic experiments, BA-1 and BA-2, was designed to prevent rapid mineral dissolution artifacts during reaction initiation, while the observed changes in the dissolved SiO_2 concentration over time is a result of secondary mineral formation. Indeed, the latter is precisely why we monitor the $^{29}\text{Si}/^{28}\text{Si}$ ratio of the solution rather than solely the dissolved SiO_2

concentrations, because the $^{29}\text{Si}/^{28}\text{Si}$ tracer is not affected by secondary mineral formation while the dissolved net SiO_2 mass balance is reflective of dissolution and precipitation effects (see SI section 1.2). Through conservative mixing relationships and by implementation of time-series changes in the concentration of dissolved SiO_2 and the associated $^{29}\text{Si}/^{28}\text{Si}$ ratio compared with the statistically constant composition of reactant basalt, the total amount of basaltic silicate dissolution can be quantified [31].

2.7 Mineral Chemistry

The speciation and distribution of Fe in the reactant natural basalt was examined by electron microprobe (EMPA) with wavelength dispersive X-ray spectroscopy (WDS), coupled with synchrotron X-ray fluorescence mapping (SXRF) and Fe K-edge (7.112 keV) X-ray absorption near edge spectroscopy (XANES) imaging. All of the crystalline basalt samples were measured in the form of polished thin sections mounted on trace-element free silica glass at the XFM beamline at the Australian Synchrotron (AS), Melbourne, Australia.

The AS is a 3 GeV ring and was operated in top-up mode with a maximum current of 200 mA. The XFM beamline has a 1.9 T wiggler source and a Si(111) monochromator with an energy resolution ($\Delta E/E$) of 1.5×10^{-4} at 10 keV. Kirkpatrick-Baez mirrors were used to focus the beam to a spot size of $\sim 2 \times 2 \mu\text{m}^2$, and each sample was measured at high resolution, oversampling with $1 \mu\text{m}$ step-size. Data were acquired in backscatter-fluorescence mode using the 386-elements Maia fluorescence detector [32]. XANES images were constructed by collecting maps at 94 monochromator energy points across the Fe K-edge [33]. Fe K-edge XANES data were also collected on a number of natural and synthetic Fe-bearing minerals, glauconite, celadonite,

ferrihydrite, and goethite, which were used to qualitatively constrain the interpretation of differences in Fe oxidation state and secondary mineral speciation.

The SXRF data and XANES images were analysed with GeoPIXE, using the dynamic analysis (DA) method to project quantitative elemental images from the full fluorescence spectra [34]. In GeoPIXE, XANES spectra can be extracted from regions selected by the user, or based on the ratios of specific energies in the XANES spectra. Selected XANES spectra were further analyzed using *Athena*, which is part of the *HORAE* package, by background fitting and calibration of the Fe K-edge energy [35].

3. Results

3.1 Mineral chemistry

Characterization of the reactant crystalline basalt, recovered from the axis of the Juan de Fuca Ridge, by EMPA analysis demonstrates that PO_4^{3-} is present in primary silicates and secondary minerals at trace levels, between 0.01-0.4 wt. % as P_2O_5 , and EMPA maps indicate that P is also concentrated within secondary minerals along the reaction rims around primary silicates. EMPA imaging and X-ray fluorescence maps coupled with Fe X-ray absorption spectroscopy measurements demonstrate that the reaction rims of the primary silicates are composed of secondary Fe^{3+} -oxide minerals that are intermixed with clay minerals (Fig. 1 and 2). The CBD reductive dissolution treatment, specifically designed to remove pre-existing Fe^{3+} -oxides associated with the partial oxidation of the reactant basalt at the seafloor, indicates that PO_4^{3-} and other components highly associated with Fe^{3+} -oxides, such as Mn, V, and Ni, are concentrated in the leachate, [1, 36-38] (Table A2). Dissolved Al^{3+} is also concentrated in the leachate, suggesting

that the dissolution of Fe^{3+} -bearing clays also occurred upon the CBD leach of the reactant basalt. The combination of these results suggests that the observed differences in the mobility of dissolved PO_4^{3-} with reaction progress between the anoxic experiments, BA-1 and BA-2, is likely attributable to the presence of pre-existing Fe^{3+} -oxide minerals associated with the reactant basalt. To circumvent this effect on dissolved PO_4^{3-} mobility, the anoxic experiment BA-1 used reactant basalt that had pre-existing secondary Fe^{3+} -oxide minerals removed by the CBD reductive dissolution treatment prior to commencement of the experiment.

3.2 Time-series changes in solution chemistry

The oxidation state of the experimental system determines the fate of Fe, either dissolved in solution as an Fe^{2+} -species or as an Fe^{3+} -oxide mineral, and is critical with respect to the mobility and bioavailability of PO_4^{3-} liberated from primary silicates upon partial dissolution. In the oxygenated basalt weathering experiments, BA-3, BA-4, and BA-5, the mobility of dissolved Fe^{2+} and PO_4^{3-} is limited (Table A1 and Fig. A1), where dissolved Fe^{2+} , ultimately derived from the dissolution of primary silicate minerals, remained below the detection limit while the initially elevated concentration of dissolved PO_4^{3-} decreased with reaction progress as a consequence of adsorption onto pre-existing and incipiently formed Fe^{3+} -oxide minerals. Interestingly, the quantitative removal of dissolved PO_4^{3-} is not complete as a consequence of the surface sites of the Fe^{3+} -oxide minerals becoming increasingly saturated with respect to other competing adsorbed dissolved species, such as SiO_2 [39, 40]. Further description of the changes in major element solution chemistry for the oxygenated and anoxic experiments is provided in the SI.

The most significant difference between the anoxic and oxygenated experiments is the increase in concentration of dissolved Fe^{2+} and PO_4^{3-} into the synthetic anoxic seawater (Fig. 3a), in stark contrast to the oxygenated experiments, where the mobility of dissolved Fe^{2+} is limited due to quantitative oxidation as Fe^{3+} -oxide minerals and the effective removal of dissolved PO_4^{3-} by adsorption (Fig. A1). Comparison between the separate anoxic experiments, BA-1 (w/ CBD) and BA-2 (w/o CBD), suggests that pre-existing Fe^{3+} -oxide minerals, formed from partial alteration of primary basalt minerals by seawater, have retained a fraction of adsorbed PO_4^{3-} prior to the experiment (Table 1 and Fig. 3a). Further, PO_4^{3-} and the trace redox-sensitive metals, V and Mn, are all highly concentrated in the CBD leachate, consistent with the high affinity of these elements for adsorption and incorporation within Fe^{3+} -oxide minerals, respectively [1, 36, 37] (Table A2). These observations may help elucidate the observed differences in dissolved PO_4^{3-} and Fe^{2+} mobility between BA-1 and BA-2, as shown by the enhanced release of these components into solution upon commencement of the reaction for experiment BA-2 [38].

The change in the $^{29}\text{Si}/^{28}\text{Si}$ ratio for experiments BA-1 and BA-2 are consistent with each other, where both decrease from approximately 100 to values between 11 and 14 due to the dissolution of reactant basalt and mixing of isotopically natural SiO_2 into the enriched $^{29}\text{SiO}_2$ -bearing synthetic seawater solution (Table 1 and Fig. 3b). The consistency between the experiments lends confidence, despite the dynamic changes in the bulk concentration of the dissolved components, Mg^{2+} , Ca^{2+} , and $\text{SiO}_2(\text{aq})$ with reaction progress, that the change in the $^{29}\text{Si}/^{28}\text{Si}$ ratio is reflective only of primary mineral dissolution (Table A1). Interestingly, both experiments asymptotically approach an elevated value, 11-13, relative to what is predicted by SiO_2 mass balance constraints of the system, where it is expected for the $^{29}\text{Si}/^{28}\text{Si}$ in solution to ultimately approach the natural

abundance $^{29}\text{Si}/^{28}\text{Si}$ ratio of ~ 0.05 . This limited mixing of SiO_2 derived from basalt into the synthetic seawater is likely due to the formation of a passivating layer of secondary minerals on the primary minerals in the basalt, effectively hindering continued reaction.

The differences in the observed dissolved PO_4^{3-} and Fe^{2+} time-series concentration data, for BA-1 and BA-2, relative to the calculated total amount of PO_4^{3-} liberated upon dissolution of primary basalt, by utilization of the time-series $^{29}\text{Si}/^{28}\text{Si}$ mass balance calculations, is shown in Fig. 4 and in Table 1. Importantly, experiment BA-1, demonstrates a 1:1 linear relationship with the calculated amount of total PO_4^{3-} liberated from basalt into solution with respect to the observed changes in ΣPO_4^{3-} with reaction progress. These time-series data, together with thermodynamic constraints, demonstrate that Fe-P phosphorous minerals, such as vivianite, do not reach a critical saturation state required for nucleation and dissolved PO_4^{3-} concentrations are not limited by adsorption partitioning onto clays upon primary silicate mineral dissolution. Experiment BA-2, however, which did not utilize the reductive dissolution pre-treatment, demonstrates significant scatter of PO_4^{3-} time-series data relative to what is expected for PO_4^{3-} released from $^{29}\text{Si}/^{28}\text{Si}$ mass balance calculations, indicating an additional source of PO_4^{3-} to the experimental solution from the basalt reactant, likely attributed to chemical exchange of the reactant solution with the adsorbed species associated with pre-existing alteration product.

4. Discussion

4.1 PO_4^{3-} Mobility upon Primary Silicate Dissolution

Both anoxic basalt weathering experiments demonstrated significant mobility of both dissolved Fe^{2+} and PO_4^{3-} with continued reaction progress (Table 1 and Fig. 3a). The dissolved $^{29}\text{Si}/^{28}\text{Si}$

ratio systematically decreased with reaction progress in both experiments, indicating release of PO_4^{3-} to seawater upon partial dissolution of primary silicate minerals within the basalt substrate (Fig. 3b). These results are in stark contrast to the oxygenated basalt weathering experiments, in which dissolved Fe, derived from primary silicate minerals, remained below the detection limit while P was either removed from solution (despite high initial dissolved P levels) or remained at steady state levels throughout reaction progress as a consequence of adsorption onto pre-existing and incipiently formed Fe^{3+} -oxide minerals (Table A1 and Fig. A1). This suggests an important dichotomy between oxygenated and anoxic deep oceans in the mobilization of P to bioavailable forms during submarine basalt weathering.

The experimental data can be used to evaluate the potential of submarine basalt weathering under anoxic conditions to serve as a source of bioavailable PO_4^{3-} to the deep ocean by using the time-series $^{29}\text{Si}/^{28}\text{Si}$ data to quantify the total amount of atmospheric CO_2 that would be consumed upon dissolution of primary silicate minerals in basalt. We assume a $\text{SiO}_2/\text{Alkalinity}$ ratio (Si/Alk) indicative of the composition of tholeiitic basalt, represented here for simplicity as enstatite (e.g., with Si/Alk = 1.0):



By combining the time-series changes in $^{29}\text{Si}/^{28}\text{Si}$ with the total dissolved SiO_2 of the experimental solution, we can use mass balance to quantify the total CO_2 consumed throughout the reaction progress (ΣCO_2). Specifically, For both anoxic experiments, BA-1 and BA-2, the time-series changes in the dissolved concentration of SiO_2 and $^{29}\text{Si}/^{28}\text{Si}$ ratio are coupled with the SiO_2 concentration and isotopic composition of basalt through conservative mixing relationships to calculate the amount of released SiO_2 into solution from basalt upon dissolution [31]. The total

CO₂ consumed is determined through stoichiometric relations in Reaction 1 and the calculated total SiO₂ released upon basalt dissolution (Table 1). The $\Sigma\text{PO}_4^{3-}/\Sigma\text{CO}_2$ mobility ratio is determined by the slope of the linear regression of the $\Sigma[\text{CO}_2]$ and $\Sigma[\text{PO}_4^{3-}]$ model data (e.g. Fig. 5), which yields the total bioavailable P released per mol of CO₂ consumed during anoxic submarine basalt weathering.

The experiment including the CBD reductive dissolution pre-treatment provides the most precise estimate of the $\Sigma\text{PO}_4^{3-}/\Sigma\text{CO}_2$ ratio during submarine basalt weathering under anoxic conditions, yielding a $\Sigma\text{PO}_4^{3-}/\Sigma\text{CO}_2$ value of $2.17 \pm 0.51 \mu\text{mol mmol}^{-1}$ (Fig. 5b). Importantly, our experimental results indicate that the $\Sigma\text{PO}_4^{3-}/\Sigma\text{CO}_2$ value characteristic of submarine basalt weathering under anoxic conditions is similar to that estimated for modern weathering of the continental crust (Fig. 6). This suggests that submarine basalt weathering under anoxic conditions should in many cases be roughly similar in its effectiveness at exporting bioavailable P during CO₂ consumption as the weathering of continental crust above sea level.

4.2 P-CO₂-O₂ Mass Balance Calculations

To gain insight into the large-scale implications of our experimental results, we use our derived $\Sigma\text{PO}_4^{3-}/\Sigma\text{CO}_2$ value as an input parameter for a global PO₄³⁻-CO₂-O₂ steady state mass balance model for a water-rich silicate planet on which basalt alteration is the primary CO₂ sink; such that the long-term carbon cycles are buffered entirely by weathering of the oceanic lithosphere [41, 42]. We envision this scenario as being applicable to portions of Earth's early history and to Earth-like volatile-rich exoplanet 'waterworlds' on which oxygenic photosynthesis has evolved. Conceptually, PO₄³⁻ is released to the ocean as volcanic/metamorphic CO₂ is consumed during

submarine basalt weathering, and some fraction of this bioavailable P passes through the biosphere while the remainder is scavenged (Fig. 7). This in turn leads to organic C burial and a release of O₂ to the ocean-atmosphere system. We explore a wide range of CO₂ outgassing rates, relative P mobilities, burial (sedimentary) P to organic C ratios, and P scavenging efficiencies in order to compute net O₂ production by the biosphere (Table 2). Because the values of many of these parameters are uncertain, we use a stochastic approach in order to compute a statistical distribution for possible global biospheric O₂ fluxes.

The parameters of the model are: (1) the volcanic CO₂ outgassing rate (J_{volc}), which at steady state must be balanced by CO₂ removal through either submarine weathering (fractionally expressed through f_{weath}) or photosynthetic uptake ($1-f_{weath}$); (2) the mobility ratio derived from our experiments ($\Sigma\text{PO}_4/\Sigma\text{CO}_2$), which describes the molar ratio between CO₂ consumed and PO₄³⁻ released during submarine weathering; (3) the scavenging efficiency of bioavailable PO₄³⁻ in the ocean interior (ϵ_P); and (4) the global net C/P ('Redfield') ratio for material buried from the oceans (r_{CP} ; in effect corresponding to a ratio between P buried and O₂ released to the ocean-atmosphere system) (Table 2). The net biospheric O₂ flux for any given combination of parameters (in Tmol O₂ y⁻¹) is thus given by:

$$J_{O_2} = J_{volc} \cdot f_{weath} \cdot \left[\frac{\Sigma\text{PO}_4}{\Sigma\text{CO}_2} \right] \cdot (1 - \epsilon_P) \cdot r_{CP} \quad (2)$$

The general sensitivity of biospheric O₂ flux in our model to individual control parameters is shown in Fig. A3. In our stochastic analysis, we vary the model parameters over the ranges given in Table 2, assuming uniform distributions for all parameters, and sample randomly among them ($n = 50,000$) to generate the statistical distribution of net biospheric O₂ fluxes shown in Fig. 8.

Results of our simulation indicate that fluxes of PO_4^{3-} from oceanic crust weathering can support a wide range of biospheric O_2 release rates, ranging between $\sim 10^{-1}$ to nearly 10^2 $\text{Tmol O}_2 \text{ y}^{-1}$ (Fig. 8). However, biospheric O_2 fluxes are generally high across a wide range of parameter space unless volcanic/metamorphic CO_2 outgassing is assumed to be very low. For instance, at our ‘default’ volcanic/metamorphic CO_2 outgassing rate of 10 TmolC y^{-1} our analysis yields a mean O_2 flux of $1.9 \text{ TmolO}_2 \text{ y}^{-1}$ with a 90% credible interval of $0.4\text{—}3.8 \text{ TmolO}_2 \text{ y}^{-1}$, while our ‘high-outgassing’ scenario yields a mean O_2 flux of $19.1 \text{ TmolO}_2 \text{ y}^{-1}$ with a 90% credible interval of $4.1\text{—}38.5 \text{ TmolO}_2 \text{ y}^{-1}$ (Fig. 8b). For comparison, the total net biospheric O_2 flux on the modern Earth is on the order of $\sim 10\text{--}20 \text{ Tmol O}_2 \text{ y}^{-1}$ [43], while biospheric O_2 fluxes during the Proterozoic following the initial oxygenation of Earth’s atmosphere have been estimated to be roughly $2\text{--}5 \text{ Tmol O}_2 \text{ y}^{-1}$ [44]. The volcanic/metamorphic outgassing rates of our default case are likely modest in the context of Earth’s history [17], while the rates implemented in our ‘high-outgassing’ case may be common on volcanically active planets during the first few billion years of their evolution [45]. In any case, our results strongly suggest that biospheres sustained entirely by bioavailable P released during submarine basalt weathering under anoxic conditions, including that of the earliest Earth, are potentially capable of generating extremely high biogenic gas fluxes that rival or exceed even those of the modern Earth.

Studies of Earth system evolution and conceptual models used to forecast the emergence and maintenance of biosignatures on volatile-rich exoplanets have neglected the differences in hydrothermal P cycling between oxic and anoxic systems, and have instead implicitly invoked conditions under which P is effectively scavenged through adsorption onto Fe^{3+} -oxide minerals formed from the hydration and oxidation of primary silicates in submarine basalt [46, 47]. Our

results stand in strong contrast to this prevailing conceptual model, and thus provide impetus to revisit mechanistic models for Earth's early oxygen cycle [16] and the factors regulating the oxygen cycles of volatile-rich silicate planets more generally. In particular, it will be important for future work to establish the ocean-atmosphere O₂ 'threshold' above which oxygenation of the deep oceans attenuates bioavailable P fluxes by initiating widespread Fe²⁺ oxidation within the ocean interior.

5. Conclusion

Intriguingly, existing model results indicate the possibility that atmospheric O₂ could be present at abundances that would potentially be remotely detectable without fully ventilating the deep oceans [3, 9, 44], with the implication that Earth-like terrestrial planets with water inventories greater than that of Earth could be very promising targets in the search for exoplanet biosignatures [2]. In any case, our experimental results provide strong evidence that fluxes of bioavailable P on terrestrial planets dominated by submarine basalt weathering under anoxic conditions are likely to be very robust and in some cases may surpass those of even the modern Earth system. Anoxic submarine weathering should thus be considered an important component of the large-scale redox balance of terrestrial planets.

Data availability

The authors declare that all solution chemistry and mineral characterization data generated and used during this study are included within the paper and its associated supplementary information.

Acknowledgements

DDS was primarily funded through the Flint Postdoctoral Fellowship provided by Yale University. We also acknowledge the Australian Synchrotron (AS) for awarding beam-time to DDS, BE, JB (AS-Proposal #13283).

Author Contributions

DDS and CTR equally contributed to this manuscript. DDS, CTR, and NJP wrote the manuscript. DDS designed and performed the experiments, with equally enthusiastic assistance by TTI, CH, JAK. CTR and TTI developed and performed the P-CO₂-O₂ mass-balance model simulations. BMT performed the thermodynamic modeling for dissolved P-speciation. BE and JB were essential for successful synchrotron XRF/XAS analysis.

References

- [1] Berner RA. (1973) Phosphate removal from sea water by adsorption on volcanogenic ferric oxides. *Earth and Planetary Science Letters*, **18**, 77-86.
- [2] Zeng L, Jacobsen SB, Sasselov DD, Petaev MI, Vanderburg A, Lopez-Morales M, Perez-Mercader J, Mattsson TR, Li G, Heising MZ, Bonomo AS, Damasso M, Berger TA, Cao H, Levi A and Wordsworth RD. (2019) Growth model interpretation of planet size distribution. *Proc Natl Acad Sci U S A*, **116**, 9723-9728.
- [3] Reinhard CT, Olson SL, Schwietermann EW and Lyons TW. (2017) False negatives for remote life detection on ocean-bearing planets: Lessons from the early Earth. *Astrobiology*, **17**, 287-297.
- [4] Erb TJ, Kiefer P, Hattendorf B, Günther D and Vorholt JA. (2012) GFAJ-1 is an arsenate-resistant phosphate-dependent organism. *Science*, **337**, 467-470.
- [5] Reaves ML, Sinha S, Rabinowitz JD, Kruglyak L and Redfield RJ. (2012) Absence of detectable arsenate in DNA from arsenate-grown GFAJ-1 cells. *Science*, **337**, 470-473.
- [6] Laakso TA and Schrag DP. (2018) Limitations on Limitation. *Global Biogeochemical Cycles*, **32**, 486-496.
- [7] Derry LA. (2015) Causes and consequences of mid-Proterozoic anoxia. *Geophysical Research Letters*, **42**, 8538-8546.
- [8] Laakso TA and Schrag DP. (2014) Regulation of atmospheric oxygen during the Proterozoic. *Earth and Planetary Science Letters*, **388**, 81-91.
- [9] Reinhard CT, Planavsky NJ, Gill BC, Ozaki K, Robbins LJ, Lyons TW, Fischer WW, Wang C, Cole DB and Konhauser KO. (2017) Evolution of the global phosphorus cycle. *Nature*, **541**, 386-389.
- [10] Ruttenger KC. (2003) The Global Phosphorus Cycle. *Treatise on Geochemistry*, **8**, 585-643.
- [11] Coogan LA and Gillis KM. (2013) Evidence that low-temperature oceanic hydrothermal systems play an important role in the silicate-carbonate weathering cycle and long-term climate regulation. *Geochemistry, Geophysics, Geosystems*, **14**, 1771-1786.
- [12] Wheat CG, McManus J, Mottl MJ and Giambalvo E. (2003) Oceanic phosphorus imbalance: Magnitude of the mid-ocean ridge flank hydrothermal sink. *Geophysical Research Letters*, **30**, 1895-1899.
- [13] Poulton SW and Canfield DE. (2011) Ferruginous Conditions: A Dominant Feature of the Ocean through Earth's History. *Elements*, **7**, 107-112.
- [14] Song H, Jiang H, Poulton SW, Wignall PB, Tong J, Song H, An Z, Chu D, Tian L, She Z and Wang C. (2017) The onset of widespread marine red beds and the evolution of ferruginous oceans. *Nat Commun*, **8**, 399-406.
- [15] Bjerrum CJ and Canfield DE. (2002) Ocean productivity before about 1.9 Gyr ago limited by phosphorus adsorption onto iron oxides. *Nature*, **417**, 159-162.
- [16] Mills B, Lenton TM and Watson AJ. (2014) Proterozoic oxygen rise linked to shifting balance between seafloor and terrestrial weathering. *Proc Natl Acad Sci U S A*, **111**, 9073-9078.
- [17] Krissansen-Totton J, Arney GN and Catling DC. (2018) Constraining the climate and ocean pH of the early Earth with a geological carbon cycle model. *Proc Natl Acad Sci U S A*, **115**, 4105-4110.
- [18] Koritnig S. (1965) Geochemistry of phosphorus - I. The replacement of Si⁴⁺ by P⁵⁺ in rock-forming silicate minerals. *Geochimica et Cosmochimica Acta*, **29**, 361-371.
- [19] Watson BE. (1980) Apatite and phosphorus in mantle source regions: An experimental study of apatite/melt equilibria at pressures to 25 kbar. *Earth and Planetary Science Letters*, **51**, 322-335.
- [20] Mehra OP and Jackson ML. (1958) Iron oxide removal from soils and clays by a dithionite-citrate system buffered with sodium bicarbonate. *Clays and Clay Minerals*, **7**, 317-327.
- [21] Herschy B, Chang SJ, Blake R, Lepland A, Abbott-Lyon H, Sampson J, Atlas Z, Kee TP and Pasek MA. (2018) Archean phosphorus liberation induced by iron redox geochemistry. *Nat Commun*, **9**, 1346-1353.
- [22] Nilsson N, Lovgren L and Sjöberg S. (1992) Phosphate complexation at the surface of goethite. *Chemical Speciation and Bioavailability*, **4**, 121-130.
- [23] Coogan LA, Daeron M and Gillis KM. (2019) Seafloor weathering and the oxygen isotope ratio in seawater: Insight from whole-rock $\delta^{18}\text{O}$ and carbonate $\delta^{18}\text{O}$ and $\Delta 47$ from the Troodos ophiolite. *Earth and Planetary Science Letters*, **508**, 41-50.
- [24] Gruber C, Harpaz L, Zhu C, Bullen TD and Ganor J. (2013) A new approach for measuring dissolution rates of silicate minerals by using silicon isotopes. *Geochimica et Cosmochimica Acta*, **104**, 261-280.
- [25] Liu Z, Rimstidt JD, Zhang Y, Yuan H and Zhu C. (2016) A stable isotope doping method to test the range of applicability of detailed balance. *Geochemical Perspective Letters*, **2**, 78-86.

- [26] Chemtob SM, Rossman GR, Young ED, Ziegler K, Moynier F, Eiler JM and Hurowitz JA. (2015) Silicon isotope systematics of acidic weathering of fresh basalt, Kilauea Volcano, Hawaii. *Geochimica et Cosmochimica Acta*, **169**, 63-81.
- [27] Bethke CM, Farrell B and Yeakel S. (2018) The Geochemist's Workbench® Release 12.0 - Reaction Modeling Guide.
- [28] Kong X-Z, Tutolo BM and Saar MO. (2013) DBCreate: A SUPCRT92-based program for producing EQ3/6, TOUGHREACT, and GWB thermodynamic databases at user-defined T and P. *Computers & Geosciences*, **51**, 415-417.
- [29] Shock EL, Sassani DC, Willis M and Sverjensky DA. (1997) Inorganic species in geologic fluids: Correlations among standard molal thermodynamic properties of aqueous ions and hydroxide complexes. *Geochimica et Cosmochimica Acta*, **61**, 907-950.
- [30] Al-Borno A and Tomson MB. (1994) The temperature dependence of the solubility product constant of vivianite. *Geochimica et Cosmochimica Acta*, **58**, 5373-5378.
- [31] Criss RE. (1999) *Principles of stable isotope distribution*, Oxford University Press, New York.
- [32] Li K, Etschmann BE, Rae N, Reith F, Ryan CG, Kirkham DH, Howard D, Rosa DRN, Zammit C, Pring A, Ngothai Y, Hooker A and Brugger J. (2016) Ore petrography using megapixel X-ray imaging: Rapid insights into element distribution and mobilization in complex Pt and U-Ge-Cu ores. *Economic Geology*, **111**, 487-501.
- [33] Etschmann BE, Brugger J, Howard D, de Jonge M, Paterson D, Naidu R, Scheckel KG, Ryan C and Lombi E. (2014) Speciation mapping of environmental samples using XANES imaging. *Environmental Chemistry*, **11**, 341-350.
- [34] Fisher LA, Fougereuse D, Cleverley JS, Ryan CG, Micklethwaite S, Halfpenny A, Hough RM, Gee M, Paterson D, Howard DL and Spiers K. (2015) Quantified, multi-scale X-ray fluorescence element mapping using the Maia detector array: application to mineral deposit studies. *Mineralium Deposita*, **50**, 665-674.
- [35] Ravel B and Newville M. (2005) ATHENA, ARTEMIS, HEPHAESTUS: data analysis for X-ray absorption spectroscopy using IFEFFIT. *Journal of Synchrotron Radiation*, **12**, 537-541.
- [36] Friedrich AJ, Scherer MM, Bachman JE, Engelhard MH, Rapponotti BW and Catalano JG. (2012) Inhibition of trace element release during Fe(II)-activated recrystallization of Al-, Cr-, and Sn-substituted goethite and hematite. *Environmental Science and Technology*, **46**, 10031-10039.
- [37] Friedrich AJ, Luo Y and Catalano JG. (2011) Trace element cycling through iron oxide minerals during redox-driven dynamic recrystallization. *Geology*, **39**, 1083-1086.
- [38] Nicholson K and Eley M. (1997) Geochemistry of manganese oxides: metal adsorption in freshwater and marine environments. *Geological Society Special Publication*, **119**, 309-326.
- [39] Stumm W, Kummert R and Sigg L. (1980) A ligand exchange model for the adsorption of inorganic and organic ligands at hydrous oxide interfaces. *Croatica Chemica Acta*, **53**, 291-312.
- [40] Sigg L and Stumm W. (1980) The interaction of anions and weak acids with the hydrous goethite (α -FeOOH) surface. *Colloids and Surfaces*, **2**, 101-117.
- [41] Abbot DS, Cowan NB and Ciesla FJ. (2012) Indication of insensitivity of planetary weathering behavior and habitable zone to surface land fraction. *The Astrophysical Journal*, **756**, 178-191.
- [42] Kite ES and Ford EB. (2018) Habitability of Exoplanet Waterworlds. *The Astrophysical Journal*, **864**, 75-102.
- [43] Catling DC and Kasting JF. (2017) *Atmospheric Evolution on Inhabited and Lifeless Worlds*.
- [44] Ozaki K, Reinhard CT and Tajika E. (2019) A sluggish mid-Proterozoic biosphere and its effect on Earth's redox balance. *Geobiology*, **17**, 3-11.
- [45] Foley BJ and Smye AJ. (2018) Carbon cycling and habitability of Earth-size stagnant lid planets. *Astrobiology*, **18**.
- [46] Korenaga J, Planavsky NJ and Evans DAD. (2017) Global water cycle and the coevolution of the Earth's interior and surface environment. *Philosophical Transactions A*, **375**.
- [47] Unterborn CT, Desch SJ, Hinkel NR and Lorenzo A. (2018) Inward migration of the TRAPPIST-1 planets as inferred from their water-rich compositions. *Nature Astronomy*, **2**, 297-302.
- [48] Wallmann K and Aloisi G. (2012) The Global Carbon Cycle: Geological Processes. In *The Fundamentals of Geobiology*, A. H. Knoll, D. E. Canfield and K. O. Konhauser (Eds.), Blackwell Publishing Ltd.
- [49] Kump LR and Arthur MA. (1999) Interpreting carbon-isotope excursions: carbonates and organic matter. *Chemical Geology*, **161**, 181-198.
- [50] Kasting JF and Canfield DE. (2012) The Global Oxygen Cycle. In *Fundamentals of Geobiology*, A. H. Knoll, D. E. Canfield and K. O. Konhauser (Eds.), Blackwell Publishing Ltd.

Figure Captions

Figure 1: Electron microscopy maps of Al, Fe, and P from grains derived from the ground basalt sampled from the Juan de Fuca Ridge used in this experimental study. Phosphorus is concentrated along areas of the altered grains that are concentrated in Fe, which is attributed to a mixture secondary Fe³⁺-oxide minerals and clays (see Fig. 2).

Figure 2: X-ray fluorescence maps (XFM) highlighting different areas associated with specific X-ray absorption near edge structures (XANES) for the natural reactant basalt used for the experiments. The Fe K-edge XANES for area #1 is associated with primary olivine and the XANES for area #2 is predominantly associated with primary Fe- and Ti-bearing spinel minerals, such as ilmenite. The XANES of area #3 is representative of secondary Fe³⁺-oxide minerals surrounding the rims of primary silicates, as confirmed by their similarity with the XANES of the standard Fe³⁺-oxide minerals. The dashed lines represent the peak maximums for the Fe³⁺-oxide standards, ferrihydrite, and Fe²⁺-bearing olivine (area #1) in the reactant basalt.

Figure 3: Time-series solution chemistry of synthetic seawater upon reaction with seafloor basalt under anoxic conditions for experiments with (BA-1) and without (BA-2) pretreatment by a reductive dissolution procedure. (a) Dissolved PO₄³⁻ and Fe²⁺ increase with reaction progress under anoxic conditions, reflecting negligible Fe³⁺-oxide mineral formation and liberation of PO₄³⁻ derived from basalt into seawater. (b) The systematic decrease in the ²⁹Si/²⁸Si ratio of the anoxic reactant solution with time is reflective of the extent of basalt substrate dissolution throughout reaction progress. Error bars if not visible are smaller than symbol size.

Figure 4: Demonstration of P-release efficiency through the difference in the observed dissolved PO_4^{3-} time-series concentration data relative to the total amount of PO_4^{3-} liberated upon dissolution of primary basalt, calculated by utilization of the time-series $^{29}\text{Si}/^{28}\text{Si}$ mass balance calculations (Table 1). Notably, the measured time-series samples from experiment BA-1 (blue symbols) lie along a 1:1 correlation for what is expected from basalt dissolution through SiO_2 mass balance constraints, suggesting no additional source of PO_4^{3-} and that PO_4^{3-} is not removed from solution due to secondary processes, such as adsorption onto secondary clay minerals. Experiment BA-2, which did not use the CBD reductive dissolution treatment, however, demonstrates significant PO_4^{3-} scatter relative to what is expected from primary silicate dissolution, likely as a result of surface exchange with pre-existing secondary Fe-oxide and clay minerals associated with the natural basalt reactant.

Figure 5: Relationship between the amount of PO_4^{3-} released into reactant seawater and the predicted CO_2 consumed upon reaction with basalt under anoxic conditions determined from the time-series $^{29}\text{Si}/^{28}\text{Si}$ data. (a) $\Sigma\text{CO}_2 - \Sigma\text{PO}_4^{3-}$ data derived from time-series dissolved $^{29}\text{Si}/^{28}\text{Si}$ ratio and concentration of PO_4^{3-} with reaction progress from both anoxic weathering experiments with (BA-1) and without (BA-2) a reductive dissolution pre-treatment. (b) Linear least-squares regression of data from experiment BA-1 (including reductive dissolution pre-treatment), the slope of which yields our estimated mobility ratio ($\Sigma\text{PO}_4^{3-}/\Sigma\text{CO}_2$) for submarine basalt weathering under anoxic conditions. The shaded envelope and quoted error on the regression slope denote the 90% confidence interval of the regression analysis.

Figure 6: Results of a Monte Carlo analysis showing the $\text{PO}_4^{3-}/\Sigma\text{CO}_2$ value ($\mu\text{mol mmol}^{-1}$) characteristic of modern continental weathering relative to experimental results for anoxic basalt weathering. The mean modern river $\text{PO}_4^{3-}/\Sigma\text{CO}_2$ ratio is 4.2, whereas, the mean experimental $\text{PO}_4^{3-}/\Sigma\text{CO}_2$ ratio is approximately 2.2. Results indicate that submarine basalt weathering under anoxic conditions releases bioavailable P at a similar rate to modern continental weathering for the same amount of CO_2 consumed.

Figure 7: Schematic of the biogeochemical model discussed in the text. A specified volcanic flux (J_{volc}) contributes CO_2 to the ocean-atmosphere system. Some fraction of this CO_2 input (f_{weath}) is removed via low-temperature ocean crust alteration, which releases inorganic bioavailable phosphorus (P_i). This bioavailable phosphorus can be recycled through the biosphere and buried in marine sediments (green), which releases O_2 to the atmosphere, or can be scavenged by Fe-bearing mineral phases in the ocean interior (red). In the model (see Eq. 2), the fraction of bioavailable phosphorus that is removed by scavenging and the dynamics of internal P recycling (e.g., the overall ratio between P burial in sediments and O_2 release) are denoted by ε_P and r_{CP} , respectively.

Figure 8: Biospheric O_2 fluxes powered by submarine basalt weathering on anoxic Earth-like planets. Conceptually, the simulation depicts the potential flux of O_2 predicted from the balance between organic carbon burial and primary productivity fueled by bioavailable PO_4^{3-} released from the oceanic crust upon weathering under anoxic conditions. Shown in (a) are O_2 fluxes as a function of volcanic CO_2 outgassing rate under the default conditions of the model (Table 2). Blue crosses denote the low-, mid-, and high-outgassing scenarios depicted in (b). Shown in (b) are

posterior distributions of biospheric O₂ flux produced from our stochastic simulation, which is constrained by: (1) the rate of volcanic CO₂ outgassing; (2) the fraction of degassed CO₂ that is channeled through ocean crust weathering; (3) the range in $\Sigma\text{CO}_2/\Sigma\text{PO}_4^{3-}$ values characteristic of submarine basalt weathering under anoxic conditions determined from this study; (4) the relative scavenging efficiency of P under anoxic conditions; (5) the C/P burial ratio in marine sediments (see SI). Each panel is labeled by volcanic CO₂ outgassing rate. Estimated ranges for volcanic CO₂ outgassing [48, 49] and biospheric O₂ flux [43, 50] for the modern Earth [44] (dark grey boxes) and biospheric O₂ fluxes on the Proterozoic Earth (light grey box) are also shown.

Table 1. Time-series solution chemistry of the anoxic experiments, BA-1 and BA-2, $^{29}\text{Si}/^{28}\text{Si}$ mass balance, and $\Sigma\text{PO}_4^{3-} - \Sigma\text{CO}_2$ model data.

Table 1: Time-series solution chemistry of the anoxic experiments, BA-1 and BA-2, $^{29}\text{Si}/^{28}\text{Si}$ mass balance model data, and $\Delta\text{PO}_4^{3-} - \Delta\text{CO}_2$ model data.													
^aBA-1	Temp. (°C)	Soln. (g)	Time (hr)	^b [SiO ₂]	[Fe ²⁺]	[PO ₄ ³⁻]	(²⁹ Si/ ²⁸ Si) _{Aq}	^c Basalt Reacted (%)	^d [SiO ₂] Basalt	^d [Fe ²⁺] Basalt	^d [PO ₄ ³⁻] Basalt	^e Σ[CO ₂]	^{e,f} Σ[PO ₄ ³⁻]
0	25	203.00	0	483.2	0.28	0.21	74.56	0.000	0.00	0.0	0.00	0.00	0.00
1	25	200.17	2	483.0	0.54	0.22	65.84	0.002	3.35	0.6	0.01	3.35	0.01
2	25	193.36	22	486.3	1.12	0.25	40.15	0.012	17.88	3.4	0.03	17.88	0.04
3	25	188.24	68	419.4	1.69	0.26	31.75	0.015	23.01	4.5	0.04	23.01	0.05
4	25	183.08	164	412.8	2.75	0.29	21.11	0.028	43.09	8.7	0.08	43.09	0.08
5	25	177.92	238	415.9	3.12	0.25	18.27	0.033	51.20	10.7	0.10	51.20	0.04
6	25	172.85	614	484.0	4.53	0.37	14.83	0.049	76.32	16.4	0.15	76.32	0.16
7	25	165.31	851	485.8	4.92	0.39	13.29	0.055	84.20	18.9	0.18	84.20	0.18
8	25	157.01	1327	490.4	5.21	0.41	14.07	0.051	78.61	18.2	0.17	78.61	0.20
BA-2	Temp. (°C)	Soln. (g)	Time (hr)	^b [SiO ₂]	[Fe ²⁺]	[PO ₄ ³⁻]	(²⁹ Si/ ²⁸ Si) _{Aq}	^c Basalt Reacted (%)	^d [SiO ₂] Basalt	^d [Fe ²⁺] Basalt	^d [PO ₄ ³⁻] Basalt	^e Σ[CO ₂]	^{e,f} Σ[PO ₄ ³⁻]
0	25	203.70	0	469.3	0.39	0.26	81.40	0.000	0.00	0.0	0.00	0.00	0.00
1	25	201.35	2	492.0	1.78	0.31	33.26	0.018	27.48	5.1	0.05	27.48	0.05
2	25	193.44	22	482.9	3.98	0.44	31.21	0.019	29.41	5.6	0.05	29.41	0.18
3	25	188.46	68	405.0	4.28	0.33	18.97	0.033	50.19	9.9	0.09	50.19	0.07
4	25	183.13	164	414.9	5.60	0.30	15.78	0.041	63.27	12.8	0.12	63.27	0.04
5	25	177.63	238	421.7	6.17	0.38	10.59	0.067	103.19	21.5	0.20	103.19	0.12
6	25	172.24	614	474.0	8.04	0.53	12.55	0.060	92.56	19.8	0.19	92.56	0.26
7	25	164.24	851	468.0	8.58	0.56	11.82	0.061	95.10	21.3	0.20	95.10	0.30
8	25	155.63	1327	475.9	9.10	0.62	11.71	0.063	96.52	22.3	0.21	96.52	0.36

^aThe basalt reactant for experiment BA-1 had undergone a reductive dissolution CBD pretreatment to specifically remove any pre-existing Fe³⁺-oxide minerals associated with the natural basalt recovered from the seafloor. ^bThe dissolved cations/anions are reported in units of μmol/kg. ^cThe percentage of basalt reacted was calculated using conservative mixing relations using the observed time-series $^{29}\text{Si}/^{28}\text{Si}$ and [SiO₂] data and the total moles of SiO₂ and $^{29}\text{Si}/^{28}\text{Si}$ derived from the basalt reactant. ^dTotal calculated concentration of SiO₂, Fe²⁺, and PO₄³⁻, derived from basalt, expected to be released into solution upon dissolution, in units of μmol/kg (Fig. 4). ^eThe ΣPO₄³⁻/ΣCO₂ mobility ratio is determined by the slope of the linear regression of the Σ[CO₂] and Σ[PO₄³⁻] model data (Fig. 5). ^fThe Σ[PO₄³⁻] data are normalized to the concentration of dissolved [PO₄³⁻] of sample #0 from experiments BA-1 and BA-2.

Table 2. Parameters utilized in the mass balance model for estimating biospheric O₂ fluxes fueled by anoxic weathering of basaltic ocean crust.

Parameter	Description	Units	Default Value	Stochastic Range
J_{O_2}	Global biospheric O ₂ flux	TmolO ₂ y ⁻¹	—	—
J_{volc}	Volcanic CO ₂ flux	TmolC y ⁻¹	10.0	1.0 – 100.0
f_{weath}	CO ₂ weathering fraction	[dimensionless]	0.8	0.1 – 0.9
$\Sigma PO_4 / \Sigma CO_2$	P Mobility ratio	μmol mmol ⁻¹	2.2	1.5 – 2.9
ϵ_P	P scavenging efficiency	[dimensionless]	0.2	0.1 – 0.9
r_{CP}	net sediment C/P burial ratio	mol mol ⁻¹	100	50 – 1000

Figure 1

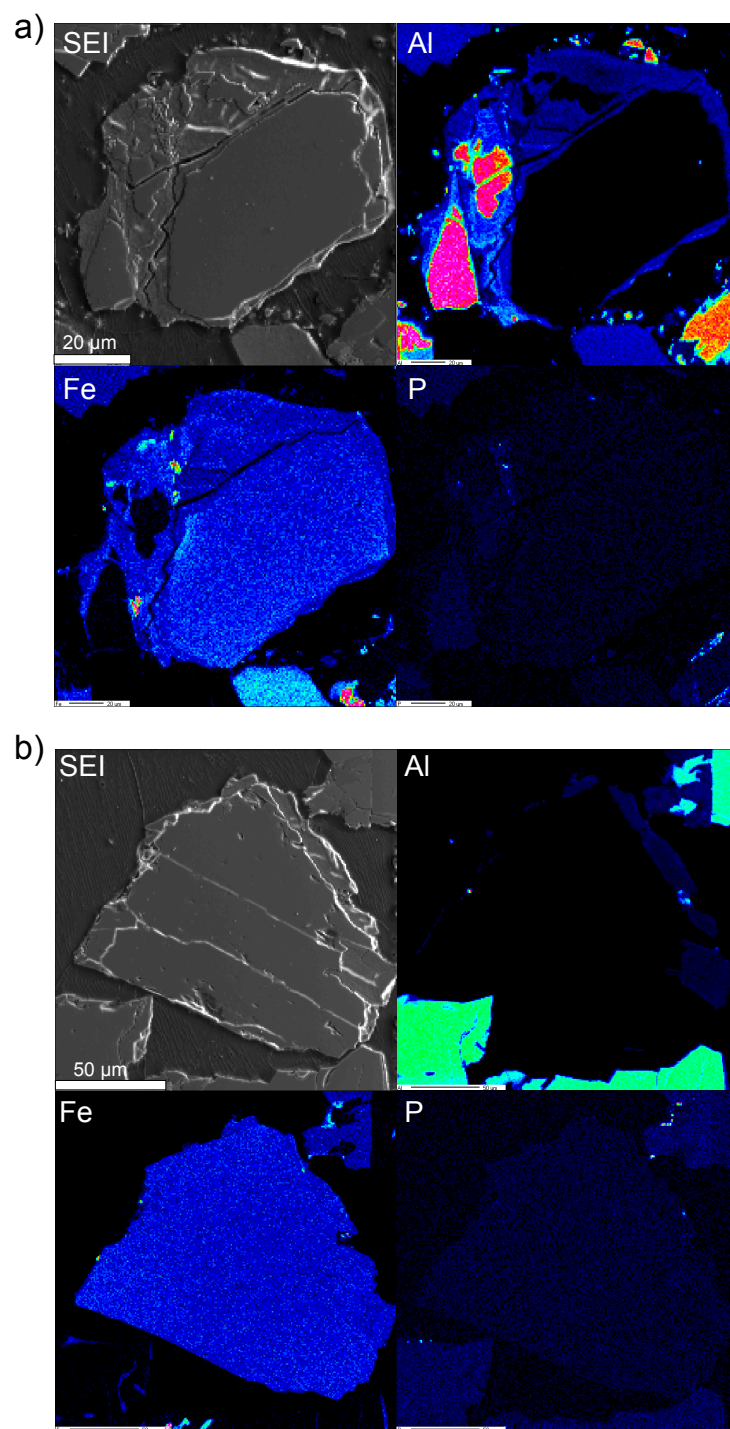
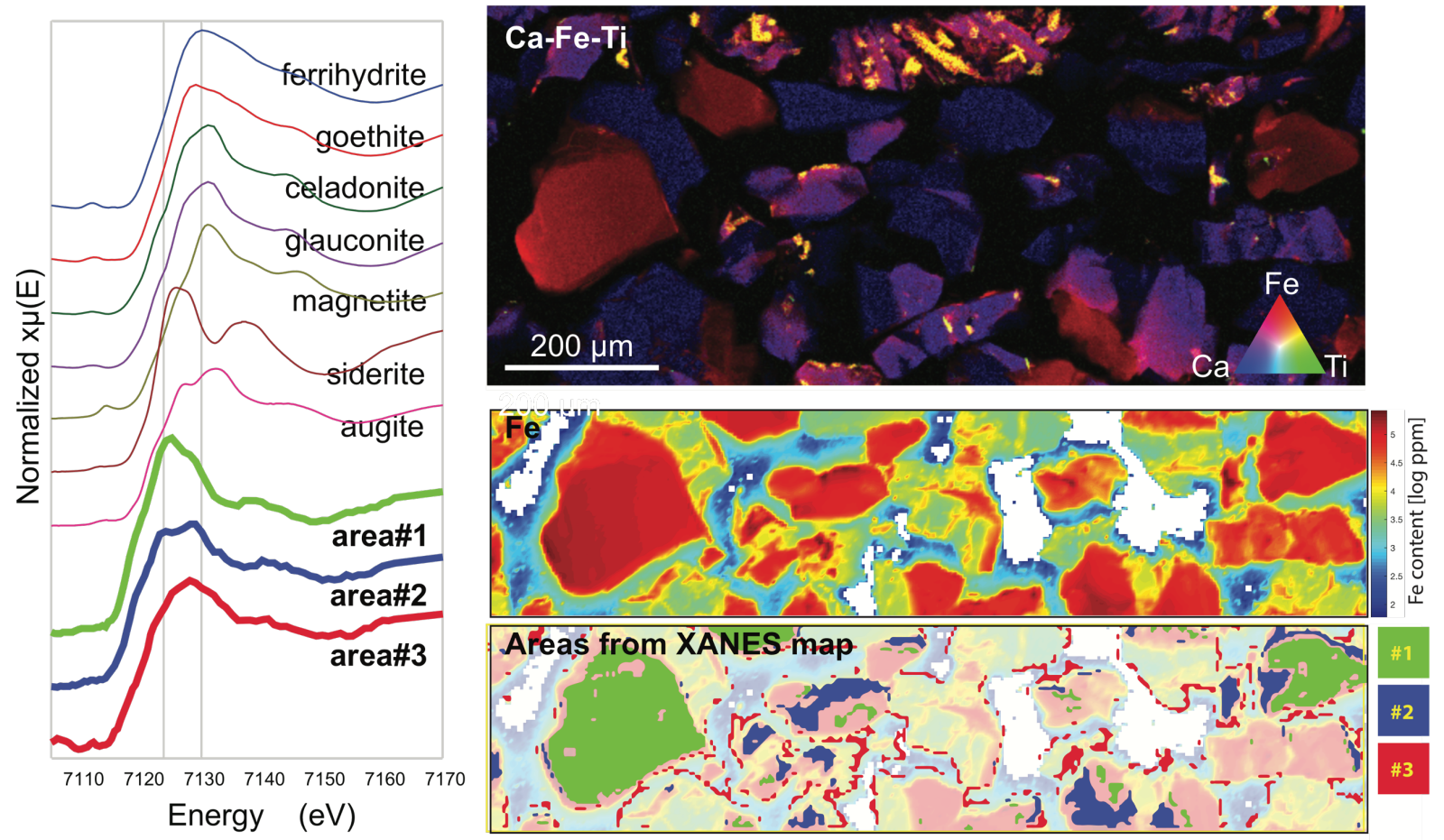
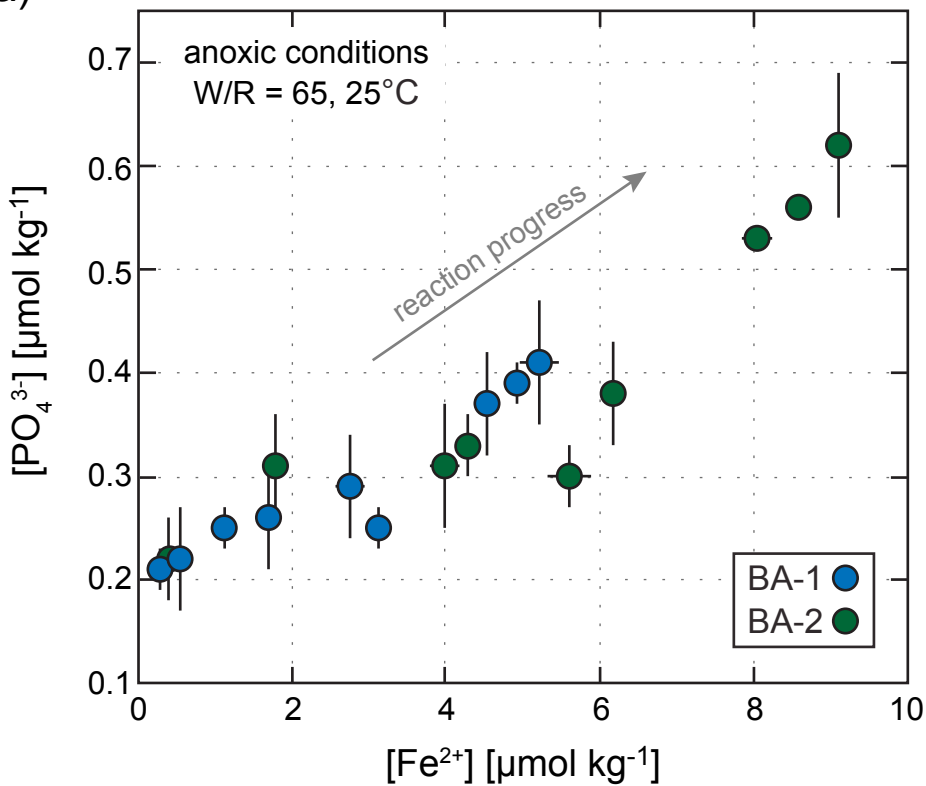


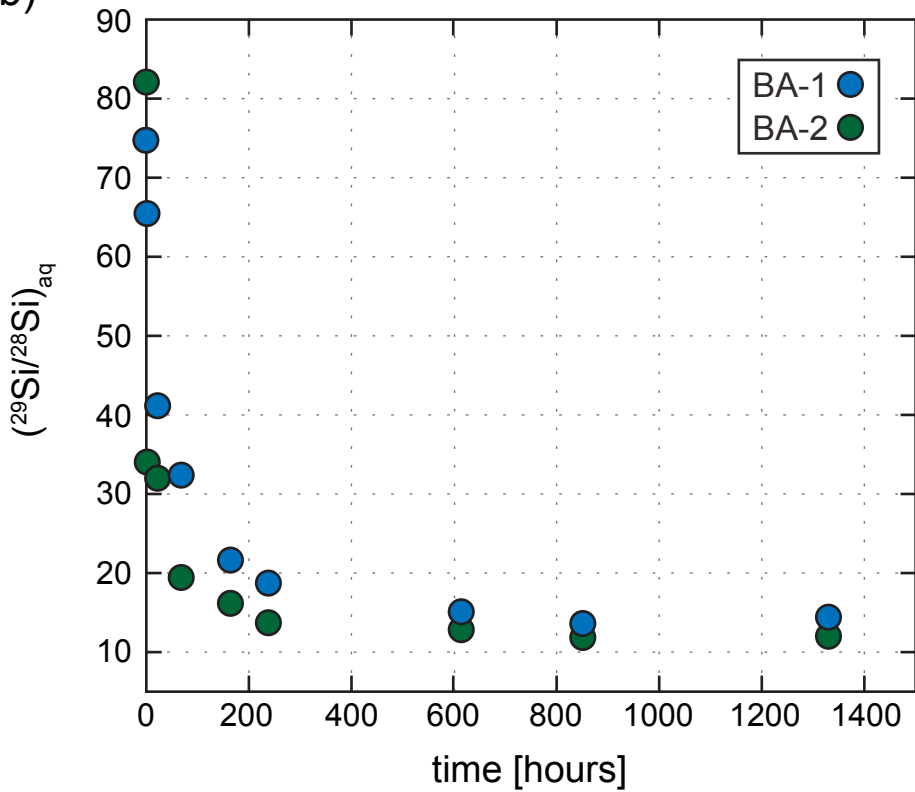
Figure 2



a)



b)



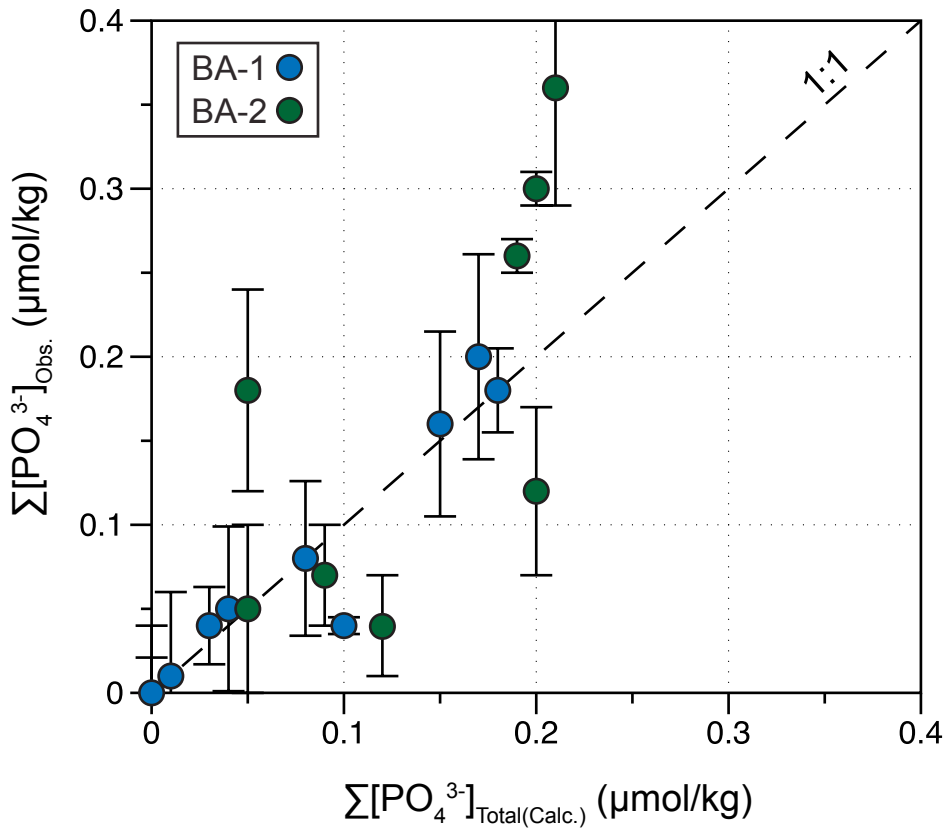
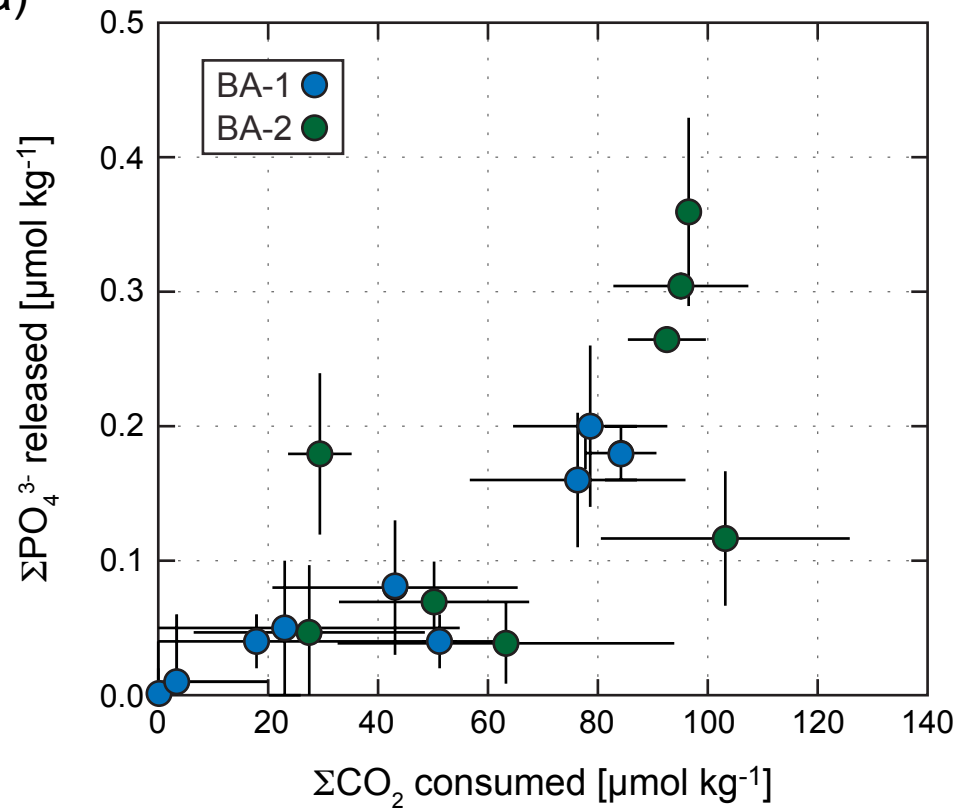


Figure 5

a)



b)

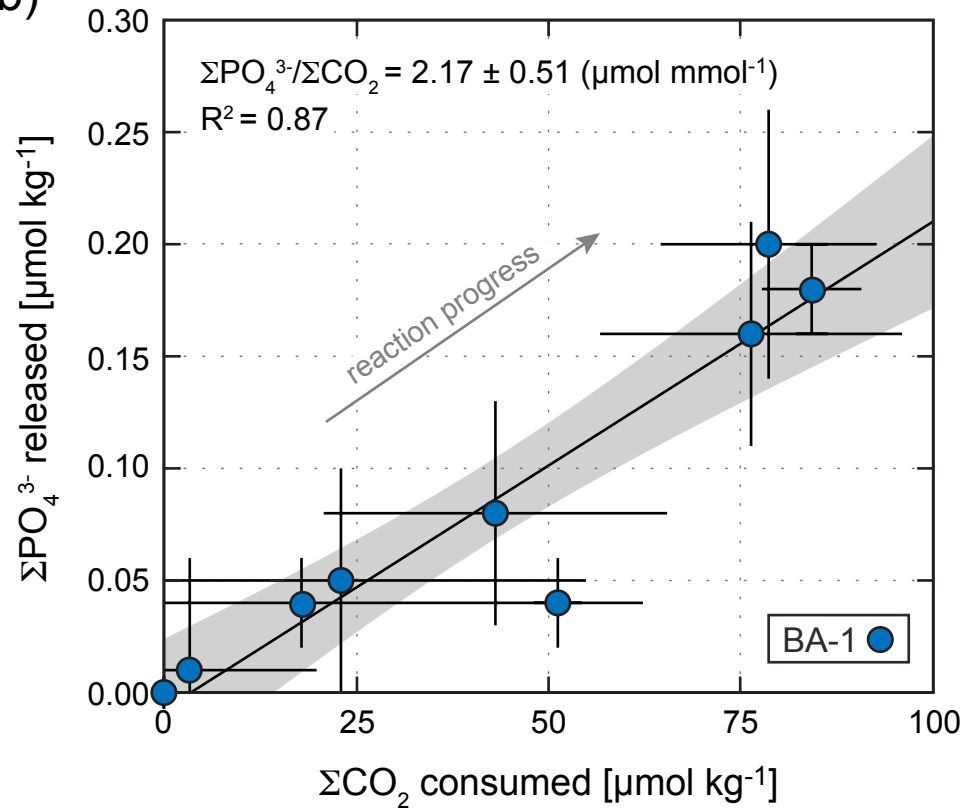


Figure 6

○ experiments

○ modern rivers

